Applied Catalysis B: Environmental 263 (2020) 118327

Contents lists available at ScienceDirect

Applied Catalysis B: Environmental

journal homepage: www.elsevier.com/locate/apcatb

A promising inorganic-organic Z-scheme photocatalyst Ag_3PO_4/PDI supermolecule with enhanced photoactivity and photostability for environmental remediation

Tao Cai[a,b,1], Wengao Zeng[a,b,1], Yutang Liu[a,b,*], Longlu Wang[c], Wanyue Dong[a,b], Hui Chen[a,b], Xinnian Xia[d]

[a] *College of Environmental Science and Engineering, Hunan University, Lushan South Road, Yuelu District, Changsha 410082, PR China*
[b] *Key Laboratory of Environmental Biology and Pollution Control (Hunan University), Ministry of Education, Lushan South Road, Yuelu District, Changsha 410082, PR China*
[c] *College of Electronic and Optical Engineering & College of Microelectronics, Nanjing University of Posts and Telecommunications, Nanjing 210023, PR China*
[d] *College of Chemistry and Chemical Engineering, Hunan University, Changsha 410082, PR China*

ARTICLE INFO

Keywords:
Ag_3PO_4
PDI
Inorganic-organic composite
Z-scheme photocatalyst
Environmental remediation

ABSTRACT

Silver orthophosphate (Ag_3PO_4) based semiconductor photocatalysis have been widely investigated for environmental purification due to its strong oxidation ability. Yet, its poor photostability and low photoactivity hamper its extensive applications. Here, an inorganic-organic Z-scheme photocatalytic system for antibiotic degradation demonstrated high photoactivity and stability through the use of Ag_3PO_4/Perylene diimide organic supermolecule (PDIsm). The apparent rate constant of tetracycline hydrochloride (TC-H) degradation with Ag_3PO_4/PDIsm was 1.5 times that of Ag_3PO_4 and 8 times that of PDIsm. The photocatalytic activity of Ag_3PO_4/PDIsm toward TC-H still kept 65 % after four reuses, while pure Ag_3PO_4 only kept 22 %. We revealed that this high photoactivity and photostability arisen from the efficient carriers separation and the formation of direct Z-scheme junction. Importantly, this Z-scheme electron transfer pathway was confirmed by thorough experimental study and density functional theory (DFT) calculation. This work demonstrated the significant potential of Ag_3PO_4-based inorganic-organic Z-scheme photocatalyst in environmental remediation.

1. Introduction

Semiconductor-based photocatalytic technique has been regarded as a green and efficient approach to solve energy and environmental problems [1,2]. The ideal semiconductor material should exhibit: (i) high redox potentials; (ii) broad light absorption; (iii) excellent carriers separation efficiency and (iv) good stability [3]. Recently, silver orthophosphate (Ag_3PO_4) as an excellent visible light photocatalyst has attracted wide attentions because of its strong oxidation ability and high quantum efficiency [4]. It exhibits prominent photocatalytic activity in water oxidation and the degradation of organic pollutants [4,5]. However, three vital problems severely hamper its photocatalytic applications as: (i) high carrier recombination efficiency [6]; (ii) relatively low reduction potential [7] and (iii) severe photocorrosion ($4Ag_3PO_4 + 6H_2O + 12\,h^+ + 12e^- \rightarrow 12Ag + 4H_3PO_4 + 3O_2$) [8].

Ag_3PO_4 based heterojunction materials such as Ag_3PO_4/graphene [9], AgX/Ag_3PO_4 [10], Ag_3PO_4@UMOFNs [11], Ag_3PO_4@$NiFe_2O_4$ [12], etc. have been studied to address above problems. Photocatalytic activities of these Ag_3PO_4-based composites were enhanced due to the improved carriers separation efficiency. Two possible electron transfer mechanism, namely tape II heterojunction and Z-scheme heterojunction, have discovered in these composites. Compared with traditional tape II heterojunction, Z-scheme heterojunction system enable to preserve higher redox potential of photogenerated carriers, which is favourable to achieve higher photocatalytic reaction efficiency [13]. However, the actual electron transfer mechanism in Ag_3PO_4-based composites is still blurred. Additionally, most Ag_3PO_4-based hybrid system are inorganic-inorganic composite while the inorganic-organic configuration has been rarely studied. In this regard, designing a Ag_3PO_4-based inorganic-organic Z-scheme photocatalyst and providing thorough experimental and theoretical investigation on this Z-scheme photocatalyst is highly attractive, but seldom studied.

---

* Corresponding author at: College of Environmental Science and Engineering, Hunan University, Lushan South Road, Yuelu District, Changsha 410082, PR China.
E-mail addresses: liuyutang@126.com, yt_liu@hnu.edu.cn (Y. Liu).

[1] These authors contributed equally to this work.

https://doi.org/10.1016/j.apcatb.2019.118327
Received 9 June 2019; Received in revised form 17 September 2019; Accepted 18 October 2019

Organic materials have many merits, such as structural diversity and excellent optical properties compared with inorganic materials [14]. Perylene diimide (PDI) and its derivatives as a typical n-type organic semiconductors have been extensively used in sensors [15], solar cells [16], and organic field-effect transistors [17] due to its excellent electronic and optical properties. Recently, Zhu et al. reported an non-covalent self-assembled PDI supramolecular (PDIsm) which can catalyze phenol degradation with wide visible light response [18]. The PDIsm with unique one-dimensional π conjugation and polar effects displayed strong photocatalytic activity. In addition, PDIsm with negative conduction band (CB) enable electron reacted with oxygen to produce superoxide radical ($^{\cdot}O_2^-$) which can oxidizes most organic pollutants [19]. Therefore, PDIsm is a promising organic semiconductor that can combinate with Ag_3PO_4 to form Z-scheme photocatalyst. High reduction potential and wide spectral absorption of PDIsm make up for the deficiency of Ag_3PO_4. The strong oxidizing ability of Ag_3PO_4 also can be preserved after forming Ag_3PO_4/PDIsm Z-scheme junction. However, to the best of our knowledge, the synthesis, application and catalytic mechanism about Ag_3PO_4/PDIsm Z-scheme junction have been largely unexplored.

In this work, we synthesized an Ag_3PO_4/PDIsm Z-scheme photocatalyst by two-step self-assembly strategy successfully. We probe the photoactivity and stability of as-prepared catalysts by the photocatalytic degradation of tetracycline hydrochloride (TC-H). Compared with pure Ag_3PO_4, Ag_3PO_4/PDIsm Z-scheme photocatalyst showed enhanced photoactivity and photostability. The origin of this enhanced activity and stability was studied by both experimental and theoretical simulation. We revealed how this direct Z-scheme photocatalyst was formed and showed how it can improve the photoactivity and photostability of Ag_3PO_4.

2. Experimental section

2.1. Materials

Perylene-3,4,9,10-tetracarboxylic dianhydride, 3-aminopropionic acid, imidazole, triethylamine were purchased from Aladdin. Nitric acid (HNO_3), silver nitrate ($AgNO_3$), sodium dihydrogen phosphate (NaH_2PO_4), benzoquinone (BQ), isopropanol (IPA), Ethylenediaminetetraacetic acid disodium salt (EDTA) and 5,5-dimethyl-1-pyrroline Noxide (DMPO) were purchased from Sinopharm Chemical Reagent Co. Ltd. All reagents were analytically pure and used without further purification. Ultrapure water was used in whole experiment.

2.2. Synthesis of PDIsm

The synthesis of self-assembled of PDIsm followed the method of the previous report [14]. 1.376 g of perylene-3,4,9,10-tetracarboxylic dianhydride, 18 g of imidazole and 2.5 g of 3-aminopropionic acid were added into a flask and heated at 100 °C for 4 h under argon atmosphere. After cooling to room temperature, this reaction solution was transferred to 100 mL ethanol with the addition of 300 mL 2 M HCl and keep stirring overnight, which obtained PDI stock solution (Fig. S1). 834 μL triethylamine solution was added into 200mL PDI stock solution with continually stirring, and then 27.3 mL 4.0 M HNO_3 was added to obtain PDIsm (Fig. S2). Thereafter washed with ultrapure water repeatedly and the obtained sample was dried at 70 °C.

2.3. Synthesis of Ag_3PO_4/PDIsm composites

Ag_3PO_4/PDIsm were synthesized by an electrostatically driven self-assembly approach. Firstly, a certain quality of PDIsm was dispersed into ultrapure water, sonicating to obtain a PDIsm suspension. Then, an excess 0.3 M $AgNO_3$ solution was added into above PDIsm suspension with continually stirring, followed by the addition of a certain volume 0.1 M NaH_2PO_4 solution to get the Ag_3PO_4/PDIsm composites. Finally, the obtained sample was washed and dried at 70 °C.

2.4. Synthesis of Ag_3PO_4

Ag_3PO_4 was synthesized by the direct reaction of NaH_2PO_4 and $AgNO_3$ at room temperature under dark condition. The obtained sample was washed and dried at 70 °C.

2.5. Characterization

Characterization techniques used in this experiment are as follows: The scanning electron microscopy (SEM, Hitachi, S-4800), transmission electron microscopy (TEM, JEOL, JEM-2100 F), X-ray diffraction (XRD, Rigaku, Smartlab), Fourier infrared spectrometer (FITR, NICOLET, 5700), X ray photoelectron spectroscopy (XPS, Thermo Fisher Scientific, England), UV–vis diffuse-reflectance spectroscopy (DRS, Cary 300, Varian), UV–vis spectrophotometer (UV-2600), Electron spin resonance (ESR, JES FA200), photoluminescence (PL) (Hitachi F-7000) and electrochemical measurements (CHI 660C electrochemical analyzer, CHI Inc., USA). The detailed description can be found in the Supporting Information (Text S1).

2.6. Evaluation of photocatalytic performance

The photocatalytic performance of as-prepared catalysts were tested by the degradation of TC-H solution. The 300 W xenon lamp with a cut filter (> 420 nm) used as the visible light source. The reaction was carried out in a beaker using 50 mL 20 mg/L TC-H solution and 20 mg catalyst powder. The suspension solution was firstly stirred in the dark for 30 min to achieve adsorption-desorption equilibrium. During the photocatalytic reaction, 1 mL reaction solution was withdraw at a given time interval, and filtered through a 0.22 μm filter membrane to remove the catalyst. The concentration of TC-H was measured by the UV–Vis spectrophotometer at 357 nm.

2.7. Theoretical calculation

The calculations were carried out using Materials Studio (MS) program with Cambridge serial total energy package (CASTEP) code based on the density-functional theory (DFT) [20]. The structure of Ag_3PO_4 and PDI were optimized. GGA-PBE0 functional formalism was used with normconserving pseudopotentials [21]. The Monkhorst–Pack scheme was used to construct the k-point meshes for Brillouin zone sampling.

3. Results and discussion

3.1. Morphological structure investigations

PDIsm was first prepared through a self-assembly approach [14]. After hydrogelation and self-assembly, the PDIsm rods were formed by π-π stacking and hydrogen bonding (Fig. S2). Due to the polar character of PDI molecule, the intramolecular electric field was formed from perylene core to carboxyl group (Fig. S3) [18]. Therefore, Ag^+ will be absorbed on carboxyl group of PDIsm rods. After reacting with NaH_2PO_4, the Ag_3PO_4 particles will be loaded on the outside of PDIsm rods in situ (Fig. 1a). This space structure was favourable for the formation of Z-scheme system, thereby enhancing photoactivity and stability, which will be discuss detailly in mechanism section. SEM and TEM images showed the morphology of as-prepared samples (Fig. 1b–g). As shown in Fig. 1b and e, Ag_3PO_4 particles exhibited irregular particle morphology with diameters of 1–4 μm. PDIsm rods with a diameter of 0.5–1.5 μm and a length of 3–5 μm consisted of the aggregates of small nanofibers (10–30 nm in diameter and 3–5 μm in length) (Fig. 1c and f)). Fig. 1d and g showed that a small amount of

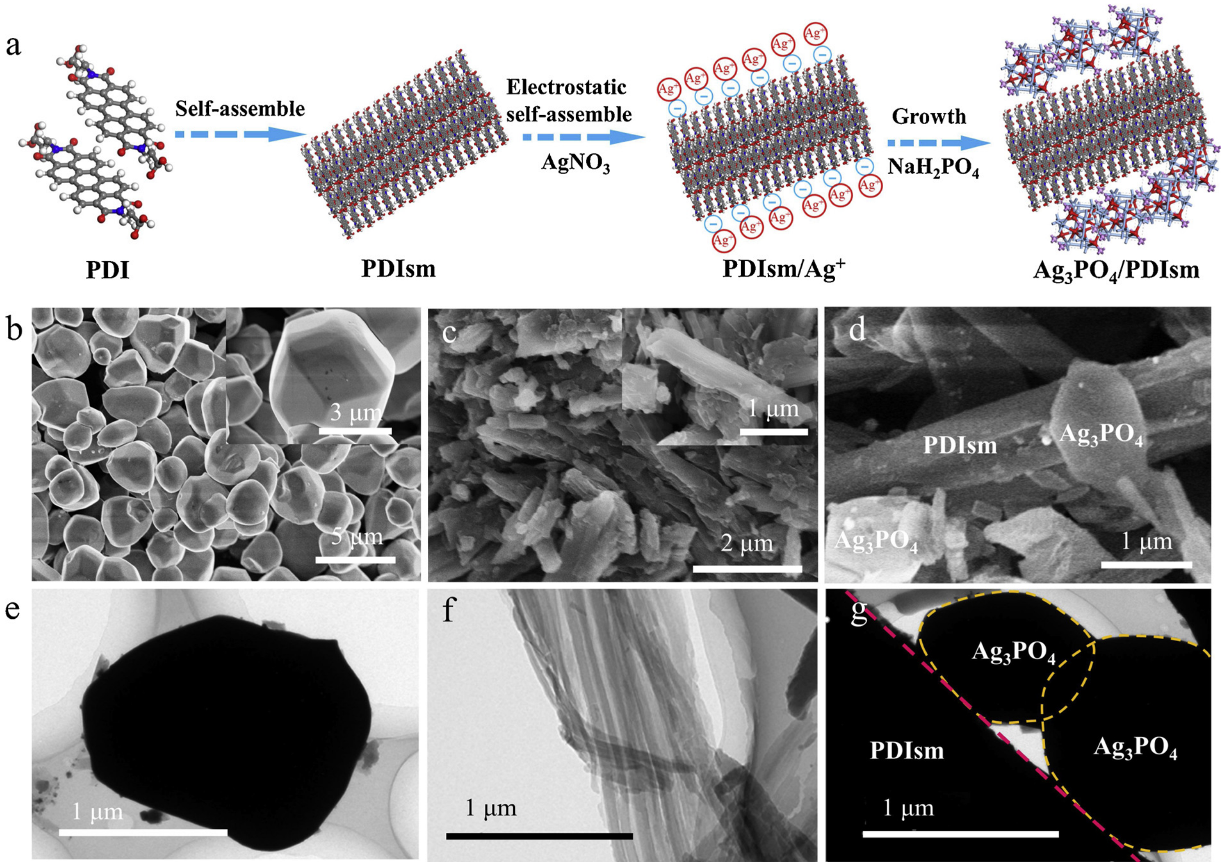

Fig. 1. Synthesis mechanism and morphology structure of as-prepared samples. (a), Schematic illustration of Ag_3PO_4/PDIsm synthesis. SEM images of (b) Ag_3PO_4, (c) PDIsm and (d) Ag_3PO_4/PDIsm composite. TEM images of (e) Ag_3PO_4, (f) PDIsm and (g) Ag_3PO_4/PDIsm composite.

Ag_3PO_4 particles were successfully loaded on the outside of PDIsm rods, which confirmed above synthesis mechanism. It should point out that we cannot further provide the high-resolution TEM image (HRTEM) of Ag_3PO_4 because it is belong to the electron beam–sensitive crystalline materials [22].

3.2. Crystallographic and chemical structure investigations

The body-centered cubic structure Ag_3PO_4 (JCPDS NO.06-0505) was observed in both Ag_3PO_4 and Ag_3PO_4/PDI sample, by XRD analysis (Fig. 2a). The weak peak at 2θ range from 10-30^0 in the PDIsm can be attributed to its characteristic diffraction peaks. The P_0 peak in the XRD pattern corresponded to the typical d spacing of π-π stacking (3.44–3.55 Å) [23]. Due to the relatively low amount PDIsm, no notable characteristic diffraction peaks of PDIsm can be detected in the XRD pattern of Ag_3PO_4/PDIsm composite. The FITR was employed to investigate the chemical structure of as-prepared samples (Fig. 2b). Ag_3PO_4 and Ag_3PO_4/PDIsm have similar FITR peaks at 550 and 1010 cm^{-1}, which can be attributed to the P—O stretching vibrations of PO_4^{3-} [24,25]. All PDIsm-based samples had typical characteristic peaks at 1688 and 1652 cm^{-1}, which were ascribed to C=O and C=C stretching vibrations, respectively [14]. The survey XPS of Ag_3PO_4 showed the presence of Ag, P, O and C (Fig. 2c). Compared with pure Ag_3PO_4, a significant signal of N1 s were found in the XPS spectrum of Ag_3PO_4/PDIsm (Fig. 2c and d), confirming the presence of PDI molecule in composite. Additionally, the high-resolution XPS (HRXPS) spectra of C1 s (Fig. 2e) and O1 s (Fig. 2f) showed the presence of additional –CONH– [26], −COOH [27] and C=O [28] group in Ag_3PO_4/PDIsm compared with Ag_3PO_4, which further confirmed the successful synthesis of Ag_3PO_4/PDIsm composite and was consistent with the FITR result. Fig. S4a and b showed the Ag 3d and P 2p spectrum of Ag_3PO_4. Two obvious peaks at 367.66 eV and 373.68 eV were ascribed to the Ag $3d_{5/2}$ and Ag $3d_{3/2}$, respectively (Fig. S4a), which can be assigned to Ag^+ of Ag_3PO_4 [29]. Moreover, P 2p peak at 132.94 eV confirmed the P^{5+} in Ag_3PO_4 (Fig. S4b) [30].

3.3. Photoelectric properties and band structure determination

The optical properties of as-prepared samples were investigated by UV–vis DRS. It can be seen that the absorption edge of Ag_3PO_4 had changed after introducing PDIsm (Fig. 3a). The absorption band edge of Ag_3PO_4 was about 525 nm while it shifted to 680 nm after introducing PDIsm and the color of sample also from yellow transformed to brown (inset in Fig. 3a). It implied that PDIsm as excellent visible light absorber can expand the photo-absorption of Ag_3PO_4. The band gap (E_g) of as-prepared samples could be evaluated by Tauc's plots (details see Text S2) [31]. As shown in Fig. 3b, the E_g of Ag_3PO_4, PDIsm and Ag_3PO_4/PDIsm were estimated to be about 2.43 eV, 1.8 eV and 1.88 eV, respectively. Mott-Schottky plot was employed to further determine the flat band potential (E_{fb}) of as-prepared samples (details see Text S3) [32]. All samples exhibited a positive slope, indicating that they are n-type semiconductors (Fig. 3c). As we known, the conduction band potentials (E_{CB}) of n-type semiconductor is more negative about 0.2 V than its E_{fb} [33]. Thus, the band structure of samples can be determined by following equations:

$$E_{CB} = E_{fb} - 0.2 \tag{1}$$

$$E_{VB} = E_g + E_{CB} \tag{2}$$

$$E_{NHE} = E_{SCE} + 0.24 \tag{3}$$

Where E_{VB}, E_{SCE} and E_{NHE} represents valence band potential, saturated calomel electrode (SCE) and normal hydrogen electrode (NHE),

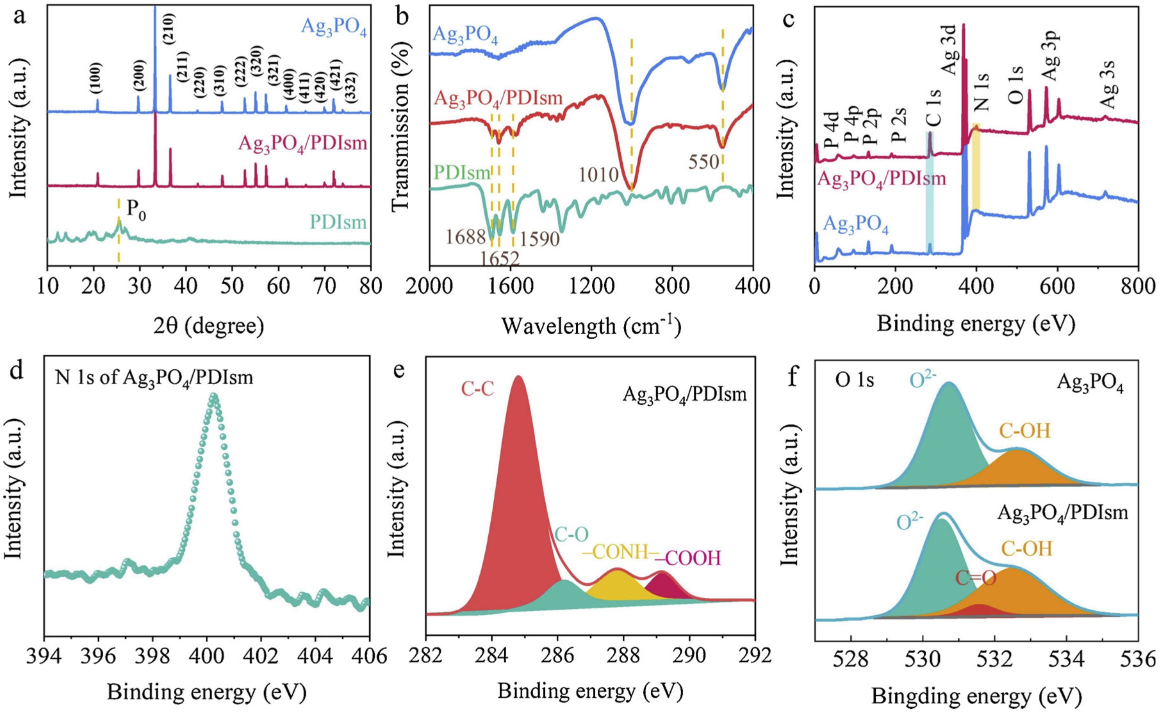

Fig. 2. Crystallographic and chemical structure characterization. (a), XRD patterns of the as-prepared samples. (b), FITR spectra of as-prepared samples. (c), Survey XPS spectrum of as-prepared samples. (d), High-resolution XPS N1 s spectrum of Ag_3PO_4/PDIsm. High-resolution XPS C 1s (e) and O 1s (f) spectrum of Ag_3PO_4 and Ag_3PO_4/PDIsm.

respectively. Therefore, the E_{CB} and E_{VB} of PDIsm were - 0.34 and 1.46 V (NHE), respectively. The E_{CB} and E_{VB} of Ag_3PO_4 were 0.27 V and 2.7 V (NHE), respectively (inset in Fig. 3c).

Fig. 3d compared the PL spectra of Ag_3PO_4 and Ag_3PO_4/PDIsm. Compared with pure Ag_3PO_4, Ag_3PO_4/PDIsm showed distinctly depressed PL emission, indicating the efficient carrier separation. This was further demonstrated by the photocurrent test (Fig. 3e). Under visible light irradiation, Ag_3PO_4/PDIsm exhibited enhanced photocurrent density compared with Ag_3PO_4 and PDIsm, suggesting that more photogenerated carriers were transferred to the surface of electrode. Electrochemical impedance spectra (EIS) Nyquist plots in Fig. 3f showed that Ag_3PO_4/PDIsm had the smallest charge transfer resistance (see the equivalent circuit in Fig. S5), indicating improved conductivity and faster electron transfer after introduction of PDIsm, which was responsible for the enhanced carrier separation efficiency. Above results demonstrated that coupling Ag_3PO_4 with PDIsm not only can expand

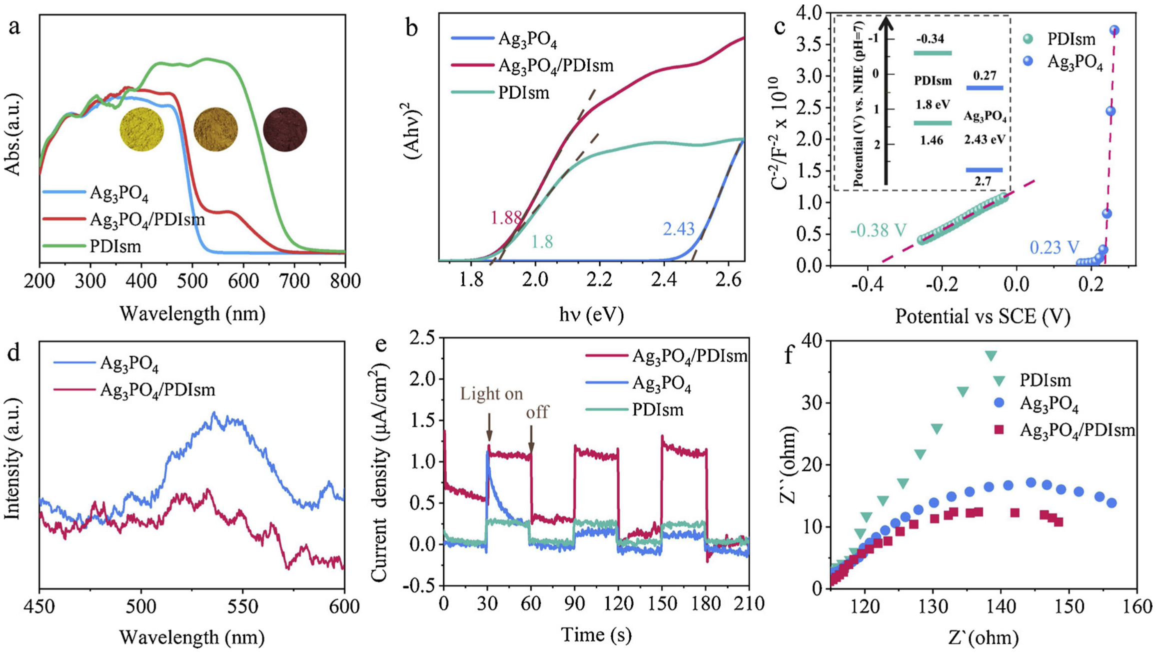

Fig. 3. Photoelectric properties and band structure characterization. (a), UV–Vis DRS of as-prepared samples. (b), The corresponding Tauc's plots. (c), Mott-Schottky plots of as-prepared samples. Inset presents the band structure of Ag_3PO_4 and PDIsm. (d), PL spectra of samples. (e), transient photocurrent responses of samples. (f), EIS Nyquist plots of samples.

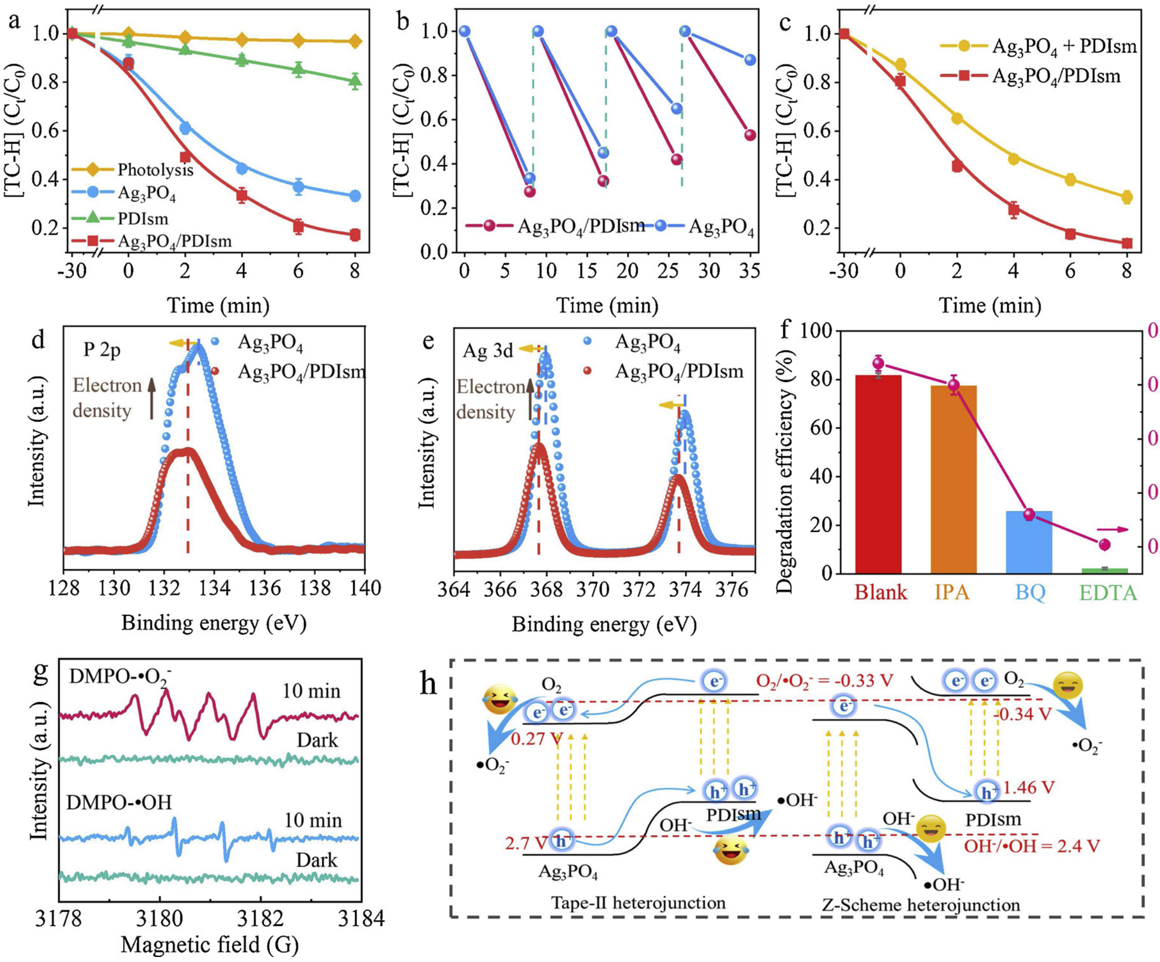

Fig. 4. Photocatalytic performance and Z-scheme mechanism. (a), Photodegradation of TC-H using as-prepared catalysts under visible light irradiation (λ > 420 nm). (b), Photodegradation of TC-H for 4 cycles using Ag_3PO_4/PDIsm and Ag_3PO_4. (c), Photodegradation of TC-H using Ag_3PO_4/PDIsm composite and physical mixture of Ag_3PO_4 and PDIsm. High-resolution XPS for P 2p (d) and Ag 3d (e) of Ag_3PO_4/PDIsm and Ag_3PO_4. (f), Photodegradation of TC-H using Ag_3PO_4/PDIsm with additions of scavengers under visible light irradiation. (g), DMPO spin-trapping ESR spectra for DMPO-˙OH and DMPO-˙O_2^-. (h), Schematic illustration of electron transfer mechanism on Ag_3PO_4/PDIsm composite.

the photo-absorption but also enhance the carrier separation efficiency, which were favourable for photocatalytic reaction.

3.4. Photocatalytic performance and Z-scheme mechanism

The content of PDIsm in composites was firstly optimized by the degradation of dye and its optimal contents was 2 wt. % (Fig. S6). The TC-H was chosen as the target pollutant to investigate the photocatalytic activity of as-prepared catalysts. As shown in Fig. 4a, the control experiment showed that the photodegradation of TC-H under visible light irradiation was negligible. In addition, pure PDIsm and Ag_3PO_4 displayed poor photocatalytic performance, where only 20 % and 66.7 % of TC-H were decomposed in 8 min, respectively. Notably, Ag_3PO_4/PDIsm presented the highest photodegradation efficiency, and nearly 82.8 % of TC-H was degraded within 8 min. The apparent rate constant of TC-H degradation ($k_{TC\text{-}H}$) was fitted by the pseudo-first-order equation [34]. We obtained $k_{TC\text{-}H}$ values of 0.023, 0.123 and 0.188 min^{-1} for PDIsm, Ag_3PO_4 and Ag_3PO_4/PDIsm, respectively (Fig. S7). The enhanced photocatalytic performance of Ag_3PO_4/PDIsm maybe origin from the pronounced carriers separation, increased visible light absorption and the formation of heterojunction. Additionally, the photostability of Ag_3PO_4/PDIsm was improved compared with pure Ag_3PO_4. The photocatalytic performance of Ag_3PO_4/PDIsm still maintained 65 % after four reuses, while Ag_3PO_4 only maintained 22 % (Fig. 4b), suggesting enhanced anti-photocorrosion performance. Additionally, we further extend the cycle times to prove the photostability of Ag_3PO_4/PDIsm. As shown in Fig. S8, a similar conclusion can be obtained. The photostability of Ag_3PO_4/PDIsm was obviously improved compared with pure Ag_3PO_4.

It is needed to ask this question. Why coupling Ag_3PO_4 with PDIsm can enhance the photocatalytic activities and stability of Ag_3PO_4? To correlate the photocatalytic activities of Ag_3PO_4/PDIsm with light absorption, the degradation of TC-H under monochromatic light irradiation was performed. However, the contribution of TC-H degradation efficiency under long wavelength monochromatic light to total degradation was a very small fraction. (Table S1). Additionally, it also can be seen from Fig. 4a that the surface adsorption was not the major factor in improving the catalytic activities in this study. Therefore, the good photocatalytic performance of Ag_3PO_4/PDIsm should mainly be attributed to enhanced carriers separation efficiency and the formation of heterojunction. The former has been demonstrated by the results of PL spectra (Fig. 3d), photocurrent test (Fig. 3e) and EIS (Fig. 3f). To revealed the role of heterojunction, control experiments, XPS analysis, radical trap experiments and ESR analysis were performed. Compared with physical mixture, Ag_3PO_4/PDIsm heterojunction displayed improved photocatalytic activities toward TC-H degradation (Fig. 4c), indicating that heterojunction played a vital role in interface electron transfer, thereby controlling the catalytic reaction process. Furthermore, in order to prove the heterojunction formed at Ag_3PO_4-PDIsm interface, a comparative experiment was carried out. The physically mixed and prepared samples were separately disperse into an aqueous solution by ultrasonication and vigorous stirring (Fig. S9a). Physically mixed samples were stratified after stopping stirring (Fig. S9b and c), indicating that physical mixed samples did not maintain the material in a uniform and stable state due to the lack of strong interaction between the interfaces. However, Ag_3PO_4/PDIsm composites all sinks to the bottom layer without stratification (Fig. S9b and c). These results strongly demonstrated that as-prepared sample formed a heterojunction with a uniform and stable state.

XPS characterization was usually used to study the surface chemistry of materials. Generally, the binding energy is negatively correlated with surface electron density [35]. The HRXPS spectra of P 2p and Ag 3d of Ag_3PO_4 and Ag_3PO_4/PDIsm were shown in Fig. 4d and e. Compared with pure Ag_3PO_4, the P 2p and Ag 3d states of the Ag_3PO_4/PDIsm moved to lower-energy position. This result indicated the transfer of electrons from PDIsm to Ag_3PO_4 at Ag_3PO_4-PDIsm interface, increasing the surface electron density of Ag_3PO_4. Combining with the band structure, we can get such a conclusion that this electron transfer mechanism will lead to the formation of an internal electric field (IEF) between the Ag_3PO_4 and the PDIsm. Specifically, the Fermi level (E_F) of PDIsm was higher than that of Ag_3PO_4. When Ag_3PO_4 coupled with PDIsm, electrons on the PDIsm will transfer to Ag_3PO_4 to get a E_F equilibrium. Thereafter, band bending in the opposite direction will occur near the Ag_3PO_4-PDIsm interface, forming the corresponding IEF (Fig. S10). Under the influence of the IEF, photogenerated electrons will transfer from Ag_3PO_4 to PDIsm, which is consistent with the direct Z-scheme mechanism. To further confirm this Z-scheme mechanism, radical trap experiment was carried out. The isopropanol (IPA), benzoquinone (BQ) and ethylenediaminetetraacetic acid disodium salt (EDTA) were used as the scavengers for $^{\cdot}OH$, $^{\cdot}O_2^-$ and h^+, respectively. The degradation performance was greatly decreased, when EDTA and BQ were added into reaction system, suggesting that h^+ and $^{\cdot}O_2^-$ were main active species (Fig. 4f). Additionally, ESR result further confirmed the production of both $^{\cdot}O_2^-$ and $^{\cdot}OH$. Under visible light irradiation, the obvious DMPO-$^{\cdot}OH$ and DMPO-$^{\cdot}O_2^-$ signals can be observed in Fig. 4g. It is known that $^{\cdot}OH$ can be produced by the oxidation of H_2O with the h^+ with an oxidation potential greater than 2.4 V vs NHE and $^{\cdot}O_2^-$ can be produced by the reduction of O_2 with e^- with an reduction potential less than –0.33 V vs NHE [36]. Therefore, the results of radical trap experiment and ESR demonstrated that the photogenerated h^+ and e^- on the Ag_3PO_4/PDIsm composite has sufficient oxidation and reduction potential for generating $^{\cdot}OH$ and $^{\cdot}O_2^-$. Therefore, the transfer of photogenerated carriers in the Ag_3PO_4/PDIsm followed the Z-scheme mechanism instead of the type-II heterojunction mechanism (Fig. 4h).

3.5. Theoretical exploration

The band structure of Ag_3PO_4 was further investigated by density functional theory (DFT) calculated (Fig. 5a and b). The optimized geometric structures of Ag_3PO_4 and PDIsm were shown in Fig. S11. As shown in Fig. 5a, the valence band (VB) top of Ag_3PO_4 was located at M point, while the conduction band (CB) bottom was located at G point. These results suggested that Ag_3PO_4 was an indirect gap semiconductor. Compared with direct gap semiconductor, the indirect gap semiconductor leaded to that the photoexcited electron need to transfer an certain distance in k-space to arrive at the VB, which can reduce the carriers recombination, thereby enhancing photocatalytic activity [37]. The E_g of Ag_3PO_4 was 2.33 eV (Fig. 5a), which consistent approximately with the experimental value 2.43 eV (Fig. 3b). Fig. 5b presented the total and partial density of states (TDOS and PDOS) of Ag_3PO_4. The bottom of its CB was mainly constituted by 4 s orbital of Ag and the top of its VB was consisted of O 2p and Ag 4d orbitals. Additionally, the dispersion of O 2p was broader than that of Ag 4d orbitals, which will be conducive to the transfer of electrons from VB to CB [21]. After coupling with PDIsm, the E_g was greatly reduced, which increased light absorption region (Fig. 5c). This results also agreed with the result of UV–vis DRS (Fig. 3a).

To further investigate the electron transfer behavior at Ag_3PO_4-PDIsm interface, we have showed the electron density difference map in the plane containing C, O, P and Ag. As shown in Fig. 5d, the electron mainly consumed around the C atom, indicating that electron tend to transfer from PDIsm to Ag_3PO_4 after formation of Ag_3PO_4/PDIsm heterojunction, which agreed with the XPS results (Fig. 4d and e). As a result, after electron diffusion between the PDIsm and the Ag_3PO_4 reach the equilibrium state, an IEF at the Ag_3PO_4-PDIsm interface will formed (Fig. 5e). Therefore, photoexcited carriers will transfer at Ag_3PO_4-PDIsm interface with the Z-scheme mechanism due to the influence of IEF (Fig. 5f). These theoretical studies confirmed previous experimental result, which further demonstrated the formation of Ag_3PO_4/PDIsm Z-scheme photocatalyst.

3.6. Photocatalytic mechanism

Fig. 6 illustrated the photocatalytic mechanism of Ag_3PO_4/PDIsm Z-scheme photocatalyst. Under illumination, the photoexcited electron prefer to transfer along the direction of quasi-one-dimensional π-π stacking, whereas holes tend to transport outside due to the polar character of PDIsm, which enhanced carriers separation efficiency. Holes in outside of PDIsm recombined with electrons of Ag_3PO_4 under the action of interface IEF. Thus, electrons accumulated at the CB of PDIsm and holes remained on the VB of Ag_3PO_4. Electrons on the CB of PDIsm with strong reduction ability can react with O_2 to produce $^{\cdot}O_2^-$ and holes on the VB of Ag_3PO_4 with strong oxidation ability can directly oxidize TC-H. Both $^{\cdot}O_2^-$ and holes were main active species for the degradation of TC-H. Moreover, because electrons in Ag_3PO_4 mainly recombined with holes in PDIsm, the reduction of Ag^+ by electrons was inhibited to a certain degree, thereby delaying photocorrosion of Ag_3PO_4.

4. Conclusion

In summary, we have demonstrated that Ag_3PO_4/PDIsm could as a promising inorganic-organic Z-scheme photocatalyst for photocatalytic application. Ag_3PO_4/PDIsm Z-scheme photocatalyst showed enhanced photoactivity and photostability compared with pure Ag_3PO_4. The apparent rate constant of TC-H degradation with Ag_3PO_4/PDIsm was 1.5 times that of Ag_3PO_4. The photocatalytic activity of Ag_3PO_4 lost 78 % after 4 cycles, while Ag_3PO_4/PDIsm only lost 35 %. The improved photocatalytic activity and stability origin from: excellent carriers separation efficiency as well as the formation of Z-scheme heterojunction at Ag_3PO_4-PDIsm interface. Importantly, XPS characterization, superoxide radical and hydroxyl radical generation test, and theoretical simulation confirmed that the formation of the IEF was intrinsic cause for the formation of this Z-scheme mechanism. This study comprehensively demonstrated the formation of direct Z-scheme junction at inorganic-organic materials interface, which can enhance photocatalytic performance and stability efficiently. It also provided an important understanding and a new vista for the development of inorganic-organic Z-scheme system.

Declaration of Competing Interest

The authors declare that they have no known competing financial interests or personal relationships that could have appeared to influence the work reported in this paper.

Acknowledgements

This work was supported by the National Natural Science Foundation of China (51872089 and 51672077), the Hunan Provincial Natural Science Foundation of China (2017JJ2026) and the Key

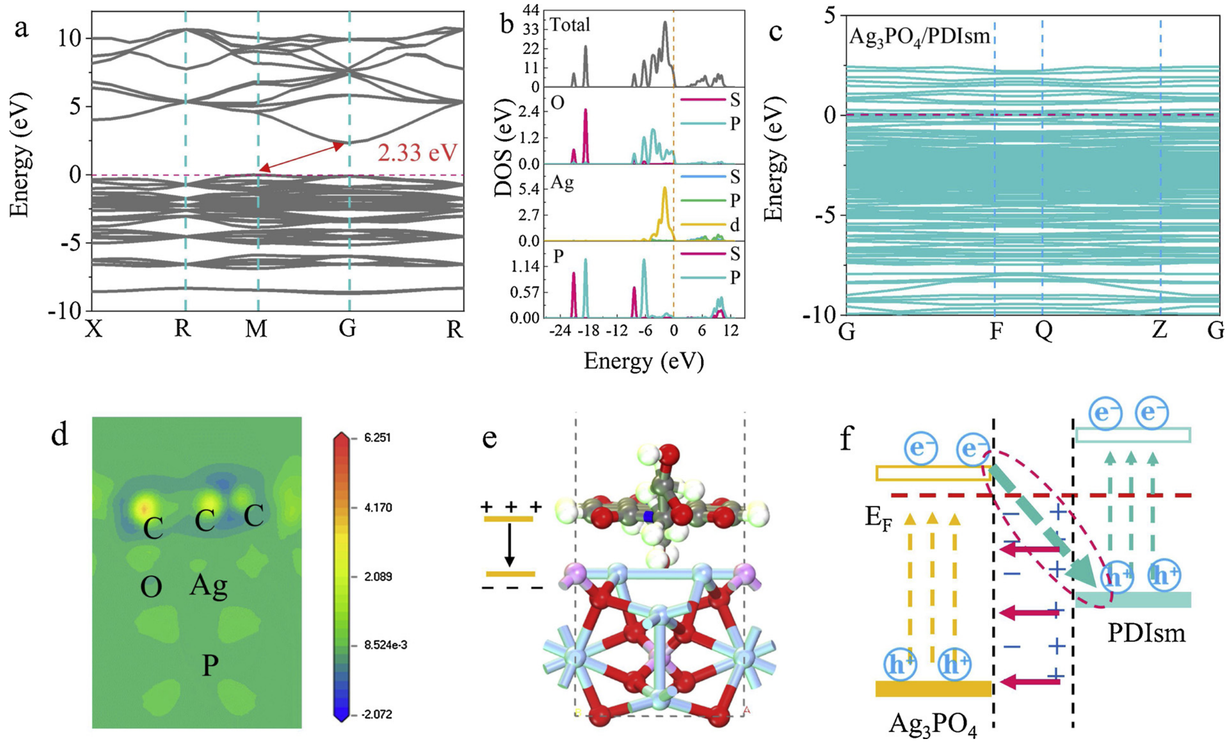

Fig. 5. Density functional theory simulation. (a), Band structure of Ag_3PO_4. The position of Fermi level is set to be 0 eV. (b), PDOS and TDOS of Ag_3PO_4. (c), Band structure of Ag_3PO_4/PDIsm composite. (d), The simulated electron-density difference of Ag_3PO_4/PDIsm composite. (e), Schematic illustration of the formation of internal electric field. (f), Schematic illustration of carrier migration on Ag_3PO_4/PDIsm under the influence of internal electric field.

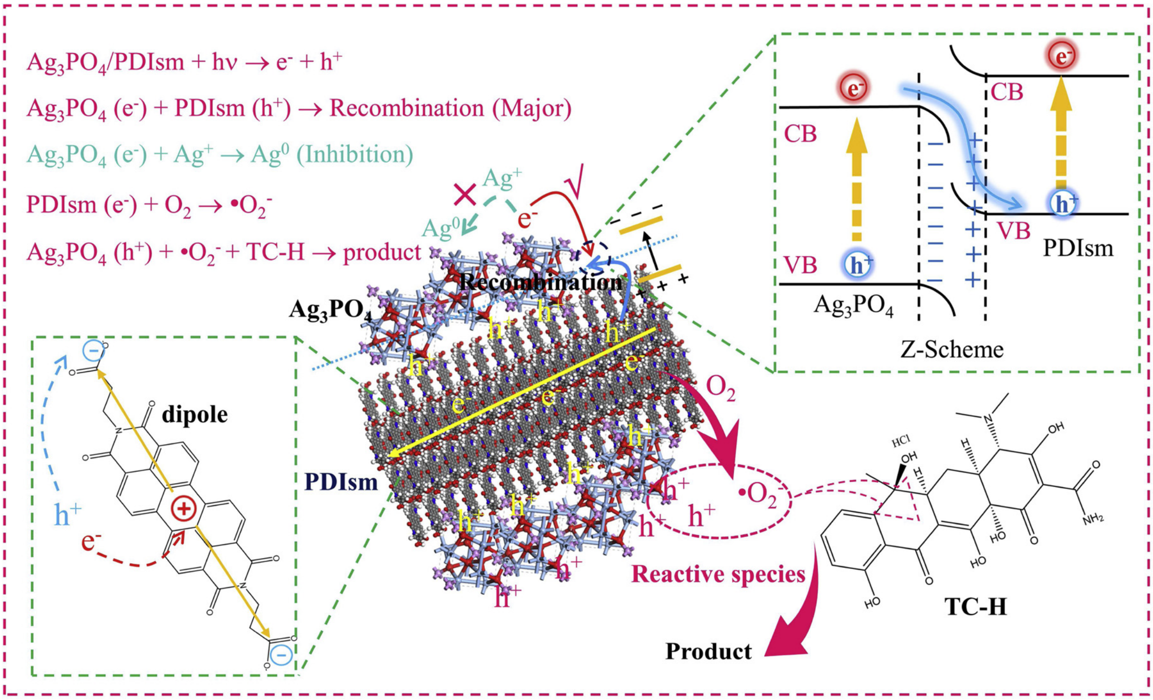

Fig. 6. Photocatalytic mechanism of Ag_3PO_4/PDIsm composite.

Laboratory of Jiangxi Province for Persistent Pollutants Control and resources Recycle (Nanchang hangkong University) (ES201880051). The authors thank National supercomputing center in Changsha for supporting this work.

Appendix A. Supplementary data

Supplementary material related to this article can be found, in the online version, at doi:https://doi.org/10.1016/j.apcatb.2019.118327.

References

[1] B.C. Hodges, E.L. Cates, J.H. Kim, Nat. Nanotechnol. 13 (2018) 642–650.
[2] D. Li, H. Zhao, L. Li, B. Mao, M. Chen, H. Shen, W. Shi, D. Jiang, Y. Lei, Adv. Funct. Mater. 28 (2018) 1806284.
[3] Y. Li, Y. Fang, Z. Cao, N. Li, D. Chen, Q. Xu, J. Lu, Appl. Catal. B 250 (2019) 150–162.
[4] Z. Yi, J. Ye, N. Kikugawa, T. Kako, S. Ouyang, H. Stuart-Williams, H. Yang, J. Cao, W. Luo, Z. Li, Y. Liu, R.L. Withers, Nat. Mater. 9 (2010) 559–564.
[5] D.J. Martin, N. Umezawa, X. Chen, J. Ye, J. Tang, Energy Environ. Sci. 6 (2013) 3380–3386.
[6] M. Sun, Q. Zeng, X. Zhao, Y. Shao, P. Ji, C. Wang, T. Yan, B. Du, J. Hazard. Mater. 339 (2017) 9–21.
[7] J. Guo, H. Zhou, S. Ouyang, T. Kako, J. Ye, Nanoscale 6 (2014) 7303–7311.
[8] Q. Xiang, D. Lang, T. Shen, F. Liu, Appl. Catal. B 162 (2015) 196–203.
[9] X. Yang, H. Cui, Y. Li, J. Qin, R. Zhang, H. Tang, ACS Catal. 3 (2013) 363–369.
[10] Y. Bi, S. Ouyang, J. Cao, J. Ye, Phys. Chem. Chem. Phys. 13 (2011) 10071–10075.
[11] Y. Liang, R. Shang, J. Lu, L. Liu, J. Hu, W. Cui, ACS Appl. Mater. Interfaces 10 (2018) 8758–8769.
[12] S. Huang, Y. Xu, T. Zhou, M. Xie, Y. Ma, Q. Liu, L. Jing, H. Xu, H. Li, Appl. Catal. B 225 (2018) 40–50.
[13] J. Low, B. Dai, T. Tong, C. Jiang, J. Yu, Adv. Mater. 31 (2019) e1802981.
[14] K. Zhang, J. Wang, W. Jiang, W. Yao, H. Yang, Y. Zhu, Appl. Catal. B 232 (2018) 175–181.
[15] M. Sauer, Angew. Chem. Int. Ed. 42 (2003) 1790–1793.
[16] L. Schmidt-Mende, A. Fechtenkötter, K. Müllen, E. Moons, R.H. Friend, J.D. MacKenzie, Science 293 (2001) 1119–1122.
[17] Y. Wen, Y. Liu, C.a. Di, Y. Wang, X. Sun, Y. Guo, J. Zheng, W. Wu, S. Ye, G. Yu, Adv. Mater. 21 (2009) 1631–1635.
[18] J. Wang, W. Shi, D. Liu, Z. Zhang, Y. Zhu, D. Wang, Appl. Catal. B 202 (2017) 289–297.
[19] P. Chen, L. Blaney, G. Cagnetta, J. Huang, B. Wang, Y. Wang, S. Deng, G. Yu, Environ. Sci. Technol. 53 (2019) 1564–1575.
[20] M. Segall, P.J. Lindan, M.a. Probert, C.J. Pickard, P.J. Hasnip, S. Clark, M. Payne, J. Phys.: Condens. Matter 14 (2002) 2717.
[21] W. Teng, X. Li, Q. Zhao, J. Zhao, D. Zhang, Appl. Catal. B 125 (2012) 538–545.
[22] M. Li, M. Chen, J. Wang, F. Teng, CrystEngComm 16 (2014) 1237–1240.
[23] A. Datar, K. Balakrishnan, L. Zang, Chem. Commun. (Camb.) 49 (2013) 6894–6896.
[24] Q. Liang, W. Ma, Y. Shi, Z. Li, X. Yang, CrystEngComm 14 (2012) 2966–2973.
[25] C. Cui, Y. Wang, D. Liang, W. Cui, H. Hu, B. Lu, S. Xu, X. Li, C. Wang, Y. Yang, Appl. Catal. B 158–159 (2014) 150–160.
[26] C. Tang, Y. Kwon, J. Leckie, J. Membrane Sci. 287 (2007) 146–156.
[27] J. Yu, W.-J. Li, H. Zhang, F. Zhou, R. Li, C.-Y. Xu, L. Zhou, H. Zhong, J. Wang, Nano Energy 57 (2019) 222–229.
[28] W. Lee, J. Lee, P. Reucroft, Appl. Surf. Sci. 171 (2001) 136–142.
[29] M. Zhu, P. Chen, M. Liu, ACS Nano 5 (2011) 4529–4536.
[30] Y. He, L. Zhang, B. Teng, M. Fan, Environ. Sci. Technol. 49 (2015) 649–656.
[31] J. Qin, X. Hu, X. Li, Z. Yin, B. Liu, K.-h. Lam, Nano Energy 61 (2019) 27–35.
[32] B. Xu, P. He, H. Liu, P. Wang, G. Zhou, X. Wang, Angew. Chem. Int. Ed. 53 (2014) 2339–2343.
[33] X. Hao, Y. Wang, J. Zhou, Z. Cui, Y. Wang, Z. Zou, Appl. Catal. B 221 (2018) 302–311.
[34] Y.-H. Chiu, Y.-J. Hsu, Nano Energy 31 (2017) 286–295.
[35] Z. Zhuang, Y. Li, Z. Li, F. Lv, Z. Lang, K. Zhao, L. Zhou, L. Moskaleva, S. Guo, L. Mai, Angew. Chem. Int. Ed. 57 (2018) 496–500.
[36] J. Low, C. Jiang, B. Cheng, S. Wageh, A.A. Al-Ghamdi, J. Yu, Small Methods 1 (2017) 1700080.
[37] M. Zhang, C. Lai, B. Li, D. Huang, G. Zeng, P. Xu, L. Qin, S. Liu, X. Liu, H. Yi, M. Li, C. Chu, Z. Chen, J. Catal. 369 (2019) 469–481.